Modeling of a large-scale magneto-rheological damper for seismic hazard mitigation. Part I: Passive mode

Yunbyeong Chae*,†, James M. Ricles and Richard Sause

[1]*ATLSS Engineering Research Center, Department of Civil and Environmental Engineering, Lehigh University, Bethlehem, PA 18015, USA*

SUMMARY

Magneto-rheological (MR) dampers are a promising device for seismic hazard mitigation because their damping characteristics can be varied adaptively using an appropriate control law. During the last few decades researchers have investigated the behavior of MR dampers and semi-active control laws associated with these types of dampers for earthquake hazard mitigation. A majority of this research has involved small-scale MR dampers. To investigate the dynamic behavior of a large-scale MR damper, characterization tests were conducted at the Lehigh Network for Earthquake Engineering Simulation equipment site on large-scale MR dampers. A new MR damper model, called the Maxwell Nonlinear Slider (MNS) model, is developed based on the characterization tests and is reported in this paper. The MNS model can independently describe the pre-yield and post-yield behavior of an MR damper, which makes it easy to identify the model parameters. The MNS model utilizes Hershel–Bulkley visco-plasticity to describe the post-yield non-Newtonian fluid behavior, that is, shear thinning and thickening behavior, of the MR fluid that occurs in the dampers. The predicted response of a large-scale damper from the MNS model along with that from existing Bouc–Wen and hyperbolic tangent models, are compared with measured response from various experiments. The comparisons show that the MNS model achieves better accuracy than the existing models in predicting damper response under cyclic loading. Copyright © 2012 John Wiley & Sons, Ltd.

1. INTRODUCTION

Magneto-rheological (MR) dampers are devices that have been successfully used to suppress vibrations in mechanical equipment, including vibration absorbers in vehicles [1, 2] and disk brakes and clutches [3]. An MR damper, shown in Figure 1, consists of a two-chamber closed system, where a piston head with an electromagnetic coil separates the two chambers. The chambers are filled with MR fluid, which passes through a small orifice between the piston head and the inner wall of the damper as the piston is stroked. The MR damper force depends on the yield stress of the MR fluid, which is a function of the magnetic field, which, in turn, is a function of the input current to the damper. When the MR fluid is subjected to a magnetic field, the iron particles in the fluid are aligned and form linear chains parallel to the field, changing the state of the fluid to a semi-solid state, which reduces the fluid viscosity and restricts the fluid movement through the orifice in the MR damper. The feasibility of using MR dampers for reducing vibrations in structures because of wind or earthquake loading has been investigated by numerous researchers [4–10]. Most of these

---

*Correspondence to: Y. Chae, ATLSS Engineering Research Center, Department of Civil and Environmental Engineering, Lehigh University, Bethlehem, PA 18015, USA.
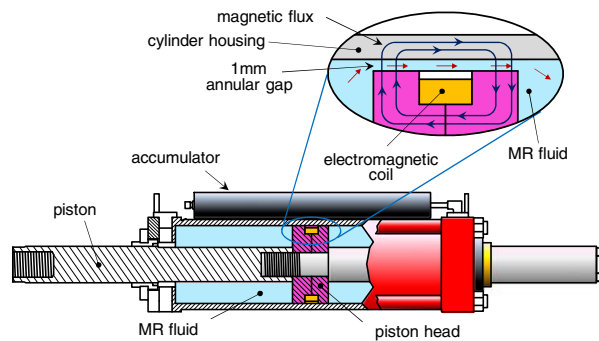†E-mail: yuc206@lehigh.edu

Figure 1. Schematic of a large-scale MR damper manufactured by Lord Corporation.

studies involved small scale MR dampers or scaled models. Effects from scaling the dampers to full scale were not investigated in these studies.

Lord Corporation (Cary, NC 27511, USA) developed its first-generation large-scale MR damper [11] in the 1990s. Yang [12] investigated the dynamic behavior of these dampers, which included several characterization tests and using the test results to calibrate a Bouc–Wen model to predict the damper response. Yang also developed a design procedure for sizing MR dampers for a building, considering the mechanics of the MR fluid and dynamic range of the dampers. However, the maximum achievable velocity in his characterization test was restricted to 0.0726 m/s because of the limited capacity of available actuators. This maximum velocity is not adequate to describe the response of dampers under design basis earthquake (DBE) or maximum considered earthquake ground motions, where the median maximum velocities of a damper in a building can exceed the velocity of 0.37 m/s and 0.54 m/s, respectively [13]. Sodeyama *et al.* [14] introduced a large-scale MR damper with a bypass-flow mechanism. In this damper, the MR fluid passes through a narrow orifice where 10 layers of electromagnetic coils are wound around the orifice to effectively generate the magnetic field. The maximum damper force they achieved was approximately 300 kN at the piston velocity of 0.4 m/s with a current input of 3.0 A. In 2005, Lord Corporation developed its second-generation large-scale MR dampers, and Bass and Christenson [15] performed characterization tests to identify the damper properties.

There are numerous models that have been developed to predict the response of MR dampers for numerical simulations. Detailed descriptions of those MR damper models can be found in the literature [16–18]. Among them, both the Bouc–Wen based model by Spencer *et al.* [16] and the hyperbolic tangent model by Gavin [18], shown in Figure 2, are often used. As shown in Figure 2 (a), Spencer *et al.* [16] combines the Bouc–Wen model with viscous dashpots and elastic springs to create a Bouc–Wen based model for an MR damper, which is referred to as the modified Bouc–Wen model. More details about these models can be found in [16] and [18]. Because of the complexity of these models, which are nonlinear, estimating the parameters for the models is a challenge. In particular, an initial estimate of the parameters must be made from prior experience or by trial and
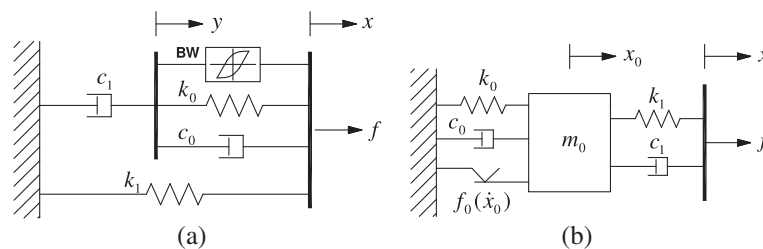

Figure 2. Mechanical MR damper models: (a) modified Bouc–Wen model and (b) Hyperbolic tangent model.

error. Moreover, because the post-yield behavior is predominantly described by a linear dashpot in both the modified Bouc–Wen and the hyperbolic tangent models, the post-yield behavior of these models is that of a Newtonian fluid where the damper force is proportional to velocity. It is difficult for these models to represent the non-Newtonian fluid behavior (i.e., the shear thinning or thickening behavior) that occurs in an MR fluid [13], especially for a post-yield response with a high velocity. Consequently, an inaccurate prediction of damper force at high velocity can occur in these models.

This paper describes a systematic modeling procedure for large-scale MR dampers. A newly developed MR damper model called the Maxwell Nonlinear Slider (MNS) model is introduced. This model is used to model large-scale MR dampers subject to realistic earthquake deformation and velocity demands. The MNS model can independently describe the pre-yield and post-yield behavior of an MR damper, which simplifies the process of identifying the parameters for the model compared with the existing models. Moreover, the MNS model can capture the non-Newtonian behavior, that is, the shear thickening or thinning behavior of the MR fluid by using Hershel–Bulkley visco-plasticity [19, 20] to describe the post-yield response of the damper. Characterization tests conducted at the Lehigh Network for Earthquake Engineering Simulation equipment site were used to identify the properties of the large-scale MR dampers, and the data was used to determine values for the parameters of the MNS model. The response from various experiments performed with the damper and the predicted response using the MNS model were compared. In this work the damper is subjected to a constant current input so the damper is in 'passive' mode. A companion paper describes the modeling of the damper in semi-active mode, where the input current is varied.

2. FORMULATION FOR MAXWELL NONLINEAR SLIDER MR DAMPER MODEL

A schematic of the MNS model is shown in Figure 3. The model is a phenomenological model with two modes: pre-yield and post-yield. In Figure 3, x is the degree of freedom of the model that is associated with the deformation of the damper, while y and z are variables associated with the pre-yield mode of the model. x and $\dot{x}$ are referred to as the damper displacement and the damper velocity, respectively. The variables x and y are related through the velocities $\dot{x}$ and $\dot{y}$, and the force f in the damper. Variables y and z are related through equilibrium with the damper force f applied to the model. As mentioned above, one advantage of the MNS model is that the pre-yield and post-yield modes of response can be separated from each other, enabling the model parameters that describe these two modes of behavior to be independently identified. A detailed explanation of the MNS model and the estimation of its parameters follows.

2.1. Pre-yield mode

In the pre-yield mode the behavior of the damper is described by a Maxwell element consisting of a dashpot with coefficient c and spring with stiffness k. The damper force f is determined by solving the following differential equation:
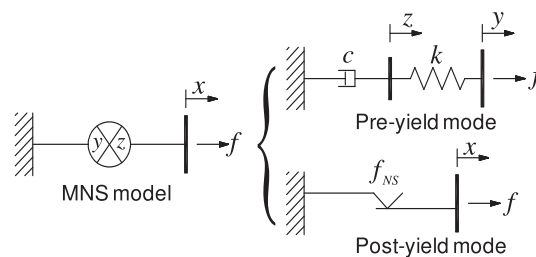

Figure 3. Maxwell Nonlinear Slider MR damper model.

$$f = k(y - z) = c\dot{z} \tag{1}$$

When the damper is in pre-yield mode, $\dot{y}$ is equal to the damper velocity $\dot{x}$. Equation (1) is solved for z using the Euler forward method to numerically integrate the differential equation, and the damper force then determined. The initial conditions for the damper have the value of y equal to x, where y remains equal to x prior to initial yielding of the damper (i.e., prior to when the damper first goes into the post-yield mode). As noted later, when the damper has yielded and is in the post-yield mode variables y and z are continuously updated by solving Equation (1) for z and yz using the damper force when the model is in the post-yield mode. When the mode subsequently changes from post-yield back to pre-yield then $y = x + \delta$, where δ is a constant during the subsequent pre-yield mode and readily calculated from the known x and y at the instant the mode change occurs. The parameters of Maxwell element can be readily estimated from the visco-elastic behavior of the MR damper, especially when the damper is subjected to small amplitude displacement and velocity. The values of c and k of the Maxwell element are obtained from the force–velocity relationship by selecting two points on the hysteretic curve and then applying visco-elasticity theory. Assuming the Maxwell element is subjected to a harmonic motion with amplitude of u_0 and circular excitation frequency of ω, the coefficients c and k are calculated as follows [21];

$$c = \frac{1}{u_0 \omega} \frac{f_0^2 + f_m^2}{f_m}, \qquad k = \frac{1}{u_0} \frac{f_0^2 + f_m^2}{f_0} \tag{2}$$

where f_0 and f_m are damper forces when the velocities are zero and maximum, respectively. Figure 4 illustrates the force–velocity relationship of Maxwell element and the definition of f_0 and f_m. Figure 5 compares the forces from the Maxwell element with the experimental measured damper forces when the damper is subjected to two different sinusoidal displacements with frequencies $f = 0.5\,\text{Hz}$ and $f = 1.0\,\text{Hz}$. The amplitude and the current input are 0.0015 m and 2.5 A, respectively, for both tests. The parameters for the Maxwell element are calculated to be $c = 11,804\,\text{kN}$ and $k = 115,000\,\text{kN/m}$ using (2) and the sinusoidal test result with $f = 1.0\,\text{Hz}$ where $f_0 = 50\,\text{kN}$ and $f_m = 80\,\text{kN}$, respectively. As can be observed from Figure 5, the Maxwell element response shows good agreement with the experimental results for both cases when $f = 0.5\,\text{Hz}$ and $f = 1.0\,\text{Hz}$. The parameters c and k can be refined using an optimization algorithm discussed later in this paper.

2.2. Post-yield mode

Experimental data from characterization tests is shown in Figure 6, where the damper force–velocity hysteretic response appears. The arrows in the figure show the path of cyclic damper force in the force–velocity plot for the case involving a frequency of $f = 3.0\,\text{Hz}$. For the other cases involving other frequencies, a similar trend was found. The solid and dashed arrows represent the paths of the

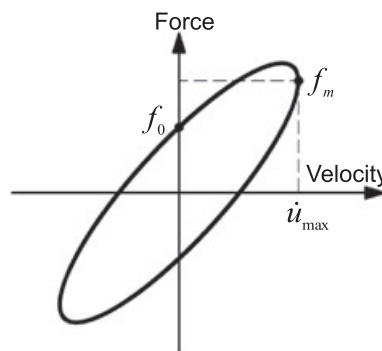

Figure 4. Force–velocity relationship of Maxwell element under harmonic motion.
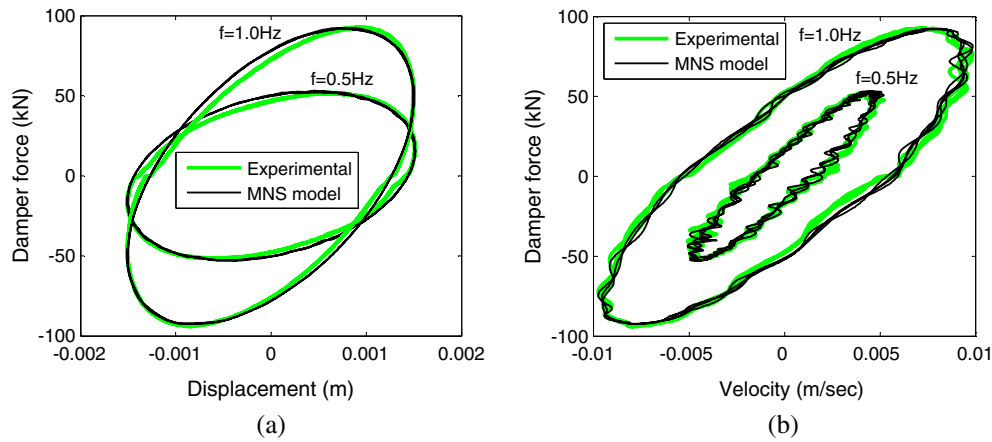
Figure 5. Comparison of pre-yield behavior of MR damper (I = 2.5A): (a) force–displacement relationship and (b) force–velocity relationship.
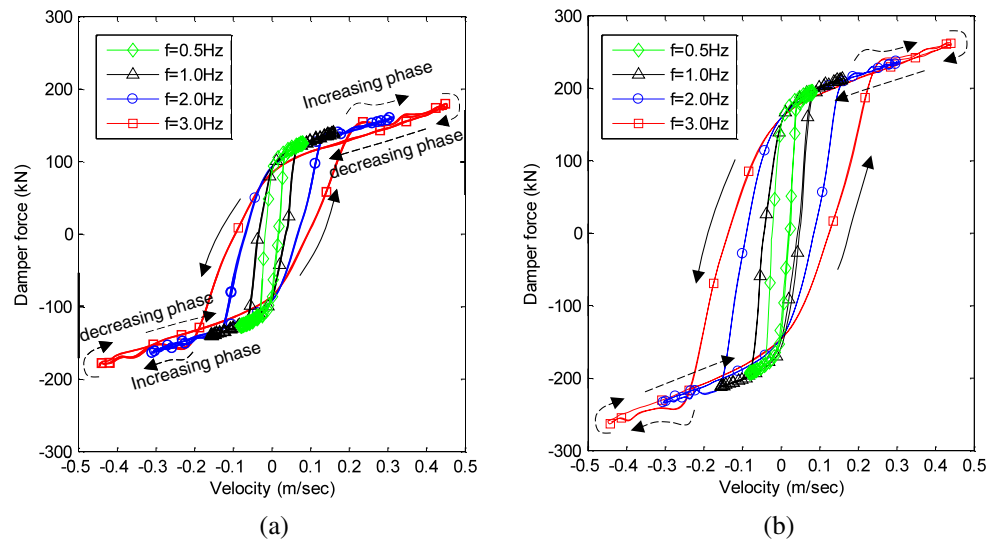

Figure 6. Experimental force-velocity relationship of MR damper under sinusoidal displacement input with various frequencies (amplitude = 25.4 mm): (a) I = 1.0A; (b) I = 2.5A.

pre-yield mode and post-yield mode, respectively. When the mode changes from the pre-yield to the post-yield, the slope of the damper force abruptly changes, enabling the mode change to be identified in the experimental data by examining the slope of the damper force in the force–velocity plot. After the mode change occurs, the damper force generally increases with increasing velocity (i.e., increasing phase). When the velocity begins to decrease after passing the maximum velocity, the damper force also decreases (i.e., decreasing phase).

The post-yield behavior of an MR damper is closely related to the damper velocity. Yang [12] showed good agreement between quasi-static measured experimental damper forces with those predicted by a model based on Hershel–Bulkley visco-plasticity theory. The quasi-static damper force is the damper force associated with a constant velocity. A damper model based on Hershel–Bulkley visco-plasticity theory can describe the shear thinning and shear thickening behavior of the MR fluid, because the theory uses a power law model [19, 20]. In the MNS model, the post-yield response of the MR damper is described by a nonlinear slider that follows a damper force trajectory (referred to as the post-yield curve), which is a function of the velocity of the damper. Figure 7
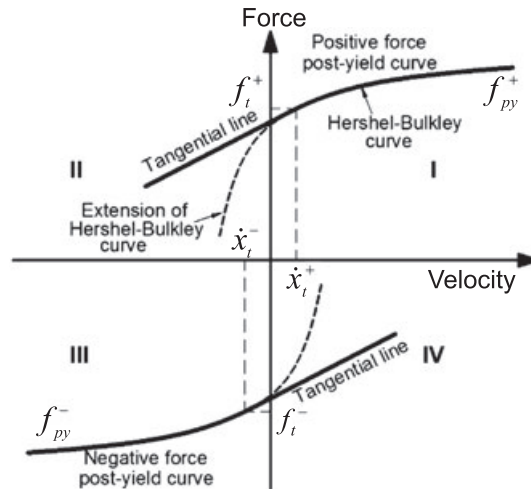
Figure 7. Predefined post-yield curves of MNS model.

shows the positive and negative post-yield curves. The post-yield curve consists of two segments: the first segment is based on Hershel–Bulkley visco-plasticity theory and the second segment is a line that is tangential to the segment defined by Hershel–Bulkley visco-plasticity theory at the velocity of $\dot{x}_t^+$ or $\dot{x}_t^-$. The mathematical representation of the positive force post-yield curve for the MNS model is given as

$$f_{\mathrm{py}}^+(\dot{x}) = \begin{cases} a + b|\dot{x}|^n & \text{if } \dot{x} \geqslant \dot{x}_t^+ \\ a_t(\dot{x} - \dot{x}_t^+) + f_t^+ & \text{if } \dot{x} < \dot{x}_t^+ \end{cases} \tag{3}$$

where a, b, n, and $\dot{x}_t^+$ are parameters to be identified, and $a_t = bn|\dot{x}_t^+|^{n-1}$, $f_t^+ = a + b|\dot{x}_t^+|^n$. The negative force post-yield curve, $f_{\mathrm{py}}^-(\dot{x})$, can be defined in a similar manner as $f_{\mathrm{py}}^+(\dot{x})$, using the appropriate values for the negative force post-yield curve parameters. MR dampers may be manufactured with imperfections whereby their force–velocity hysteretic response does not show a perfect symmetry. Thus, separately defining the post-yield curves for the positive and negative force regions in the force–velocity space can improve the accuracy of the damper model by fitting the curves to the experimental data.

The experimental post-yield curve in quadrant I (where the damper force and velocity are both positive) and III (where the damper force and velocity are both negative) in Figure 7 can be obtained from a constant velocity or a sinusoidal test. The parameters a, b, and n in (3) can be identified from the experimental data using optimization theory. Because of the simplicity of the Hershel–Bulkley model, the convergence to the final values for these parameters is not very sensitive to the initial estimate of the parameters and the procedure is completely independent of the identification of the values for c and k that describe the pre-yield mode of the MNS model. The tangential line noted above is added to define the post-yield curve in quadrants II and IV. A small positive value for $\dot{x}_t^+$ and negative value for $\dot{x}_t^-$ can be initially used and then, their values adjusted using an optimization algorithm so that the model matches the experimental data.

Identifying the post-yield curves in quadrants II and IV can be a challenging task because it is difficult to obtain the experimental post-yield data from a constant velocity test in these quadrants. In this study, the tangential lines in quadrants II and IV are used to make it easy to describe the change of mode from post-yield to pre-yield. In the MNS model, the change of mode from post-yield to pre-yield usually occurs near zero velocity. A small positive value for $\dot{x}_t^+$ can be used to minimize the distortion of the Hershel–Bulkley curve in quadrant I, but $\dot{x}_t^+$ cannot be too small because the tangential line needs to have an appropriate slope to match the experimental data observed in quadrant II. The same phenomenon exists along the path of the negative force post-yield curve in quadrants III and IV. The

parameters of $\dot{x}_t^+$ and $\dot{x}_t^-$ are determined in such a way to have the best match to the experimental damper response using an optimization method described later.

The post-yield curve is composed of two phases in the MNS model, namely, an increasing phase and decreasing phase. If the magnitude of the damper force is increasing during the post-yield mode, the damper is in the increasing phase. On the contrary, the damper is in the decreasing phase if the magnitude of the damper force is decreasing. Because the post-yield curve shows a monotonic increase or decrease in damper force with respect to the velocity $\dot{x}$, the damper is in the increasing phase when the product of damper force and damper acceleration, $\ddot{x}$,, is positive; otherwise, it is in the decreasing phase.

Experimental data from characterization tests show that the trajectory of damper forces can be slightly different during the increasing and decreasing phases. The difference between the paths for the increasing and decreasing phases can be distinctly observed in Figure 6(a) where the current is $I = 1.0\,A$. For the case of $I = 2.5\,A$, the discrepancy between the force paths in quadrant I is not as significant as that in quadrant III. This phenomenon is associated with the fluid dynamics of the MR fluid passing through the orifice and bypass valve of the damper. To account for this force discrepancy, an inertial force term is added to the post-yield damper force for the MNS model, where the damper force with the additional inertia force is given as

$$f = \begin{cases} f_{py}(\dot{x}) & \text{, increasing phase} \\ f_{py}(\dot{x}) + m_0(\ddot{x}) & \text{, decreasing phase} \end{cases} \tag{4}$$

In (4), f_{py} is either the positive or negative force post-yield curve and m_0 is a virtual mass associated with the additional inertia force. The parameter m_0 can be estimated by equating the product of the measured damper acceleration and m_0 to the experimental force discrepancy between the increasing and decreasing phases.

2.3. Criteria for mode changes

When the model is in the pre-yield mode and the damper force f from the Maxwell element reaches the post-yield curve, the nonlinear slider is activated and the mode changes from the pre-yield to the post-yield mode. Mathematically, this condition is expressed as

$$|f| = \left| f_{py}(\dot{x}) \right| \tag{5}$$

If f reaches $f_{py}(\dot{x})$, then the damper force is determined to be in the post-yield mode. Equation (5) implies that the damper force is bounded by the positive and negative post-yield curves in the MNS model. Overshooting of the damper force is avoided in the model by taking a substep that corresponds to the instant that the damper force f reaches $f_{py}(\dot{x})$ and then the response to the remaining part of the step is subsequently determined in post-yield mode.

When the model is in the post-yield mode, the transition from the post-yield mode to the pre-yield mode occurs when the following velocity equation is satisfied:

$$\dot{x} = \dot{y} \tag{6}$$

where, $\dot{y}$ is calculated from

$$\dot{y} = \frac{\dot{f}}{k} + \frac{f}{c} \tag{7}$$

Equation (7) is obtained by rearranging (1) to arrive at an expression for y in terms of f, k, and z, and then taking the time derivative of y and making use of $f = c\dot{z}$ from Equation (1). The value for $\dot{y}$ is calculated by substituting the damper force f and the time derivative of the damper force, $\dot{f}$, from the

post-yield mode into (7). To obtain a smooth transition from the post-yield mode to the pre-yield mode, the pre-yield mode variables y and z are continuously updated by solving Equation (1) for z and yz using the damper force when the model is in the post-yield mode.

3. EXPERIMENTAL SETUP FOR CHARACTERIZATION TEST

The characterization tests were performed on a large-scale second-generation MR damper, manufactured by Lord Corporation. A schematic of the damper is shown in Figure 1 and the damper specification is provided in Table I. The length and available stroke of the damper are 1.5 m and ±0.279 m, respectively. The electromagnetic coil consists of 368 turns of 18 AWG magnet wire with an annular gap of 1.0 mm between the piston head and the inside diameter of the cylinder. The damper is filled with approximately 19 L of MRF-132DG type MR fluid manufactured by Lord Corporation.

The experimental setup for the MR damper characterization tests is shown in Figures 8(a) and (b). It includes a hydraulic actuator to impose displacements on the MR damper. One end of the actuator is attached to a reaction frame (*A-frame* in Figure 8) and the other connected to the MR damper through an actuator extension consisting of a stiff steel section (*actuator extension* in Figure 8). The MR damper is secured to a tie-down beam that is anchored to the laboratory strong floor. The actuator extension is used to accommodate the spacing of anchor locations for threaded rods that secure the damper and actuator to the laboratory strong floor. The maximum force capacity of the actuator is 1700 kN; the actuator can generate approximately 500 kN of force at a piston velocity of 1.0 m/s. A 534 kN load cell is installed between the actuator extension and the damper piston to directly measure the force developed in the damper.

The current going into the damper is controlled by a pulse width modulation (PWM) type current driver manufactured by Advanced Motion Controls (Camarillo, CA 93012, USA) (30A8). To reduce the noise from the electrical power source, a Schaffner line filter is deployed in front of the DC power supply that provides 72 DC voltage to the PWM servo-amplifier. The command current is transferred to the PWM servo-amplifier through a DC voltage signal with a range of –10V to +10V to produce the desired current utilizing pulse width modulation. The current going into the MR damper is monitored by a current probe (CR Magnetics (St. Louis, MO 63122, USA) current transformer).

To monitor the temperature of the damper, four thermocouples are installed on the surface of the damper cylinder housing along the circumference at mid-length of the damper. Dyke *et al*. [4] stated that the property of the MR fluid is not sensitive to a change of temperature. However, Yang [12] reported that a 15% ~ 25% force drop was observed when the damper temperature increased from room temperature to 180°F while the damper was subjected to cyclic triangular displacement excitations. Thus, it is important to maintain the damper near ambient temperature at the start of each test to minimize the effect of temperature on the damper characterization tests. Each characterization test was performed with an initial temperature of 72°F to 75°F.

Table I. Specification for large-scale MR damper.

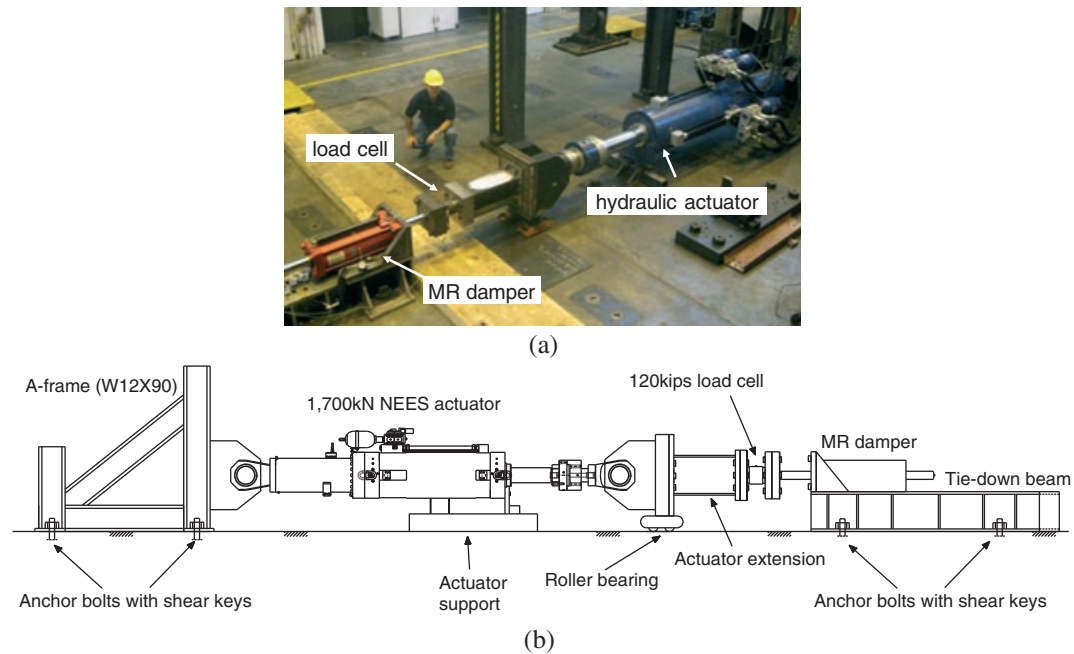| Item	Damper characteristic
Total damper length	1.5 m
Weight	280 kg
Piston diameter	0.089 m
MR fluid	MRF-132DG (approx. 19 L)
Accumulator pressure	5.2 MPa
Available stroke	±0.279 m
Cylinder diameter	0.203 m
Cylinder length	0.800 m
Electromagnetic coil	368 turns of 18 AWG magnet wire
Annular gap	0.001 m

Figure 8. Experimental setup for the characterization test of MR damper: (a) photograph and (b) schematic drawing.

4. IDENTIFICATION OF MODEL PARAMETERS

As noted above, the MR damper behavior depends on displacement, velocity, acceleration, and input current. To capture the effects of these dependencies, 24 characterization tests were conducted involving harmonic displacement histories with different frequencies and current input, where varying the frequency resulted in different maximum velocities and accelerations. The harmonic displacement histories had an amplitude of 0.0254 m and frequencies of 0.5 to 3 Hz. The current inputs ranged from 0 to 2.5 A. A summary of the values of these variables for the characterization tests is given in Table II. The maximum velocity in the harmonic tests ranges from 0.080 m/s (0.5 Hz) to 0.479 m/s (3 Hz). Each time history displacement includes a total of 10 cycles, where the first cycle is used to ramp up to the targeted displacement amplitude of 0.0254 m. Figure 9 shows an example of the applied displacement history and damper hysteretic response associated with 1 Hz harmonic loading and a 2.5 A current input.

The parameters for the MNS model were identified by minimizing the error between the response prediction by the model and the characterization data. The particle swarm optimization (PSO) algorithm was used to identify the parameters. The PSO concept is motivated by the social behavior of a swarm of animals such as a flock of birds or a school of fish [22]. In the PSO algorithm, a particle is a trial set of values for the model parameters. During the optimization the PSO algorithm results in the particles migrating towards the same set of values, which is the converged optimum solution. The PSO method is considered to be less sensitive to local minimization problems and is known to be more accurate than traditional optimization methods for identifying MR damper model parameters [23]. In

Table II. Variables for sinusoidal characterization tests.

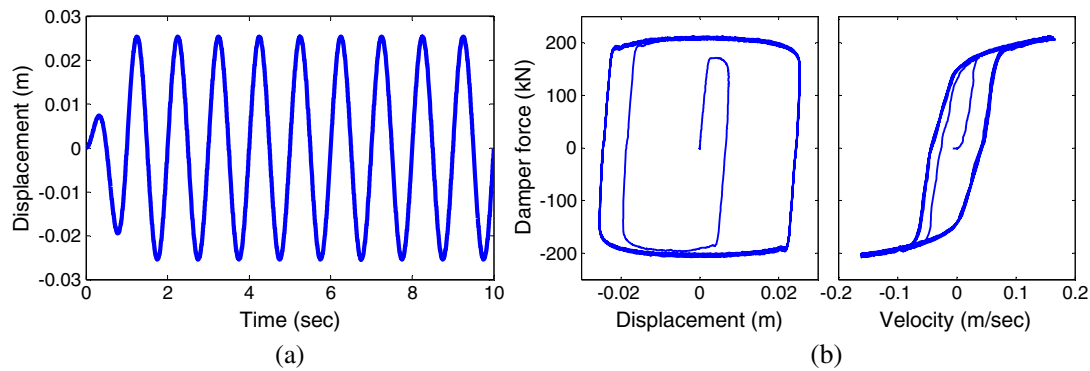| Variable	Value
Amplitude	0.0254 m
Frequency (Hz)	0.5, 1.0, 2.0, 3.0
Input current (A)	0.0, 0.5, 1.0, 1.5, 2.0, 2.5

Figure 9. Characterization test: (a) applied displacement time history and (b) damper hysteretic response, 1 Hz and 2.5 A.

this study, the normalized root mean square (RMS) error, E^{RMS}, is used as the objective function to be minimized to determine the model parameter values for a prescribed current input, where:

$$E^{RMS} = \frac{\sqrt{\sum_i^N \left(f_e(x_i, \dot{x}_i) - f_p(x_i, \dot{x}_i) \right)^2}}{\sqrt{\sum_i^N f_e(x_i, \dot{x}_i)^2}}$$

In (8), $f_e(x_i, \dot{x}_i)$ and $f_p(x_i, \dot{x}_i)$ are the experimental damper force and the predicted damper force by the damper model, respectively, at the damper displacement x_i and velocity $\dot{x}_i$. N is the number of data samples used to determine the model parameters. Data from the latter 9 cycles of the characterization tests, where the steady state response is achieved, is used in (8). If $E^{RMS} = 0$, the predicted damper force history is exactly the same as the experimental results.

Table III summarizes the identified parameters for the MNS model for various input current levels using the PSO algorithm. The initial estimates of the MNS model parameter values were based on the procedure described previously. The number of particles and the maximum iteration count for the PSO algorithm are $N_s = 50$ and $j_{max} = 150$, respectively. As noted previously, the performance of the MNS model was compared with the modified Bouc–Wen and hyperbolic tangent models. The parameters for these models are also identified using the PSO algorithm with the same experimental data set, using the same number of particles and iteration count as those for the MNS model. The identified parameters for the modified Bouc–Wen and hyperbolic tangent models are presented in Tables IV and V. In Table IV k_0, k_1, c_0, and c_1 are the values for the spring stiffness and dashpots while x_0 is the initial displacement for the x DOF shown in Figure 2(a). α, β, γ, n, and A are values for the original Bouc–Wen model of Wen [24]. In Table V, k_0, k_1, c_0, c_1, and m_0 are the values for the

Table III. Identified parameters for MNS damper model.

			Positive force post-yield curve				Negative force post yield curve				
Current	c (kN·s/m)	k (kN/m)	a (kN)	b (kN s/m)	n	$\dot{x}_t^+$ (m/s)	a (kN)	b (kN s/m)	n	$\dot{x}_t^-$ (m/s)	m_0 (kN·s²/m)
I = 0.0A	10,000	100,000	7.5	243.5	1.62	0.010	−7.3	−235.6	1.60	−0.010	0.50
I = 0.5A	11,000	100,000	53.1	162.5	0.85	0.010	−53.1	−162.5	0.85	−0.010	0.50
I = 1.0A	12,000	118,000	91.5	122.5	0.52	0.010	−96.0	−134.9	0.60	−0.010	1.60
I = 1.5A	12,000	118,000	126.7	152.1	0.58	0.010	−126.7	−152.1	0.58	−0.010	1.50
I = 2.0A	11,491	110,030	148.5	166.3	0.66	0.003	−146.8	−182.1	0.71	−0.003	1.05
I = 2.5A	12,278	112,890	138.5	161.8	0.46	0.017	−133.5	−171.8	0.46	−0.012	1.04

Table IV. Identified parameters for modified Bouc–Wen model.

Current	k_0 (kN/m)	k_1 (kN/m)	c_0 (kN·s/m)	c_1 (kN·s/m)	x_0 (m)	α (kN/m)	β (m^{-2})	γ (m^{-2})	n	A
I = 0.0A	56.09	2.94	105.0	32943	0.14	15.5	15.59	1066.8	2.27	364.7
I = 0.5A	36.68	5.32	196.9	19541	0.16	55.6	49.64	1657.6	5.27	1923.7
I = 1.0A	9.71	1.88	179.6	13551	0.21	106.0	6.34	937.3	3.20	1013.0
I = 1.5A	30.12	3.48	208.2	12224	0.02	205.4	53.62	1778.8	3.22	538.3
I = 2.0A	89.24	3.71	227.8	11445	0.17	164.3	9.10	755.1	8.07	628.1
I = 2.5A	10.36	1.21	209.0	11651	0.12	170.9	5.92	610.7	4.80	650.5

Table V. Identified parameters for hyperbolic tangent model.

Current	k_0 (kN/m)	k_1 (kN/m)	c_0 (kN·s/m)	c_1 (kN·s/m)	m_0 (kN·s^2/m)	f_0 (kN)	V_{ref} (m/s)
I = 0.0A	2.45	226,890	125.7	173.3	0.59	5.2	0.00818
I = 0.5A	1.97	99,216	188.0	287.0	1.03	58.1	0.00828
I = 1.0A	1.60	108,160	161.6	231.7	1.23	109.4	0.00718
I = 1.5A	5.16	95,592	187.3	575.2	1.49	141.9	0.01246
I = 2.0A	2.26	104,390	204.0	231.8	1.82	160.8	0.01311
I = 2.5A	4.58	100,400	186.0	563.2	1.68	174.2	0.01387

respective springs, dashpots, and mass shown in Figure 2(b), and f_0 and V_{ref} are the yield force and a reference velocity governing the sharpness of the yield function for the hyperbolic tangent model, respectively. Figure 10 illustrates the convergence of the PSO algorithm to the values for the parameters for the three damper models when the damper current is I = 2.5A. The normalized RMS error after 150 iterations is 0.0242 for the MNS model, 0.0375 for the modified Bouc–Wen model, and 0.0274 for the hyperbolic tangent model. The initial values for the modified Bouc–Wen and hyperbolic tangent models are based on the values provided in [25] and [15], respectively. Figure 10 shows that the RMS error values for the parameters for the MNS model are smaller than for the modified Bouc–Wen and hyperbolic tangent models.

5. EVALUATION OF MNS MR DAMPER MODEL UNDER CONSTANT CURRENT

Figure 11 compares the experimental quasi-static behavior of the MR damper with predictions by the MNS model. Predictions by the modified Bouc–Wen and hyperbolic tangent damper models are also
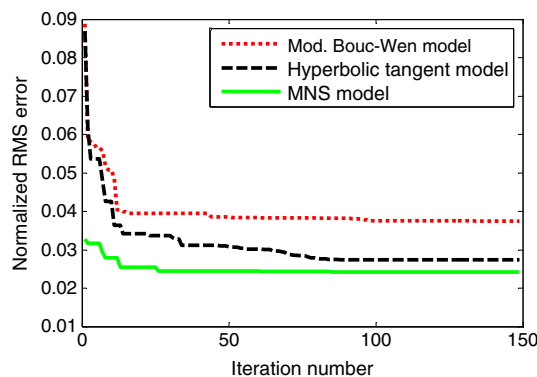

Figure 10. Convergence characteristic of normalized RMS error of damper models using PSO algorithm, I = 2.5 A.
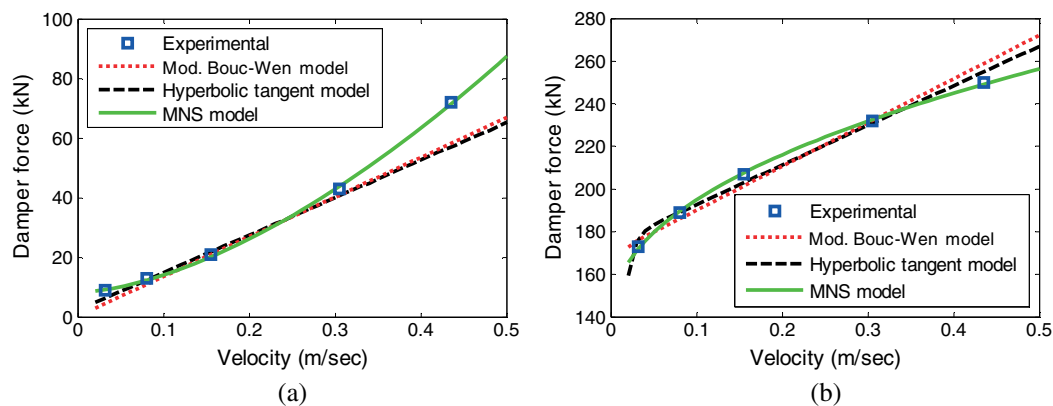
Figure 11. Quasi-static behavior of damper models and comparison with sinusoidal test results: (a) I = 0.0 A and (b) I = 2.5 A.

shown. The experimental data points shown are from five sinusoidal tests with amplitudes of 0.0254 m and frequencies of 0.2, 0.5, 1, 2, and 3 Hz, respectively. The data points identified in Figure 11 represent the measured damper force corresponding to the maximum velocity in each test (i.e., when the acceleration is zero). The curve showing the results from each model describes the quasi-static behavior of the MR damper, which as noted previously is a trace of damper force under constant velocity. It is noticeable that the experimental data for I = 0.0 A shown in Figure 11(a) has a shear thickening behavior, while the experimental data for I = 2.5 A shown in Figure 11(b) has a shear thinning behavior. The MNS model shows better agreement with the experimental data than the other models because the MNS model can account for shear thinning and shear thickening behavior. The damper force–velocity curves for the hyperbolic tangent and the modified Bouc–Wen models are almost linear and do not agree well with the experimental data.

To further validate the MNS model, the response of the MNS model under various damper displacement histories and current input described in Table VI are investigated. Figure 12 compares the damper behavior predicted by the MNS model with experimental results when the damper with an input current of I = 0.0 A was subjected to the Gaussian white noise displacement input with a bandwidth of 2 Hz (Figure 12(a)). The force–velocity response from experimental data shown in Figure 12(d) clearly indicates shear thickening behavior. Overall, the prediction by the MNS model shows good agreement with the experimental data. In Figure 13, the response of the MNS model is compared with experimental data from the Gaussian white noise displacement input with a 4 Hz bandwidth and a current input of I = 2.5 A. The experimental data for force–velocity in Figure 13(d) shows shear thinning behavior. Figure 13(d) shows that the MNS model captures this effect and accurately predicts the damper force.

The MNS model was also assessed from tests using earthquake ground motions. The assessment of MR damper models under earthquake input used a predefined displacement input, where the displacement history is obtained from a numerical simulation of the 2-story linear elastic shear building structure shown in Figure 14. In the numerical simulation, the MR dampers are analytically modeled using the MNS model with the values given in Table III to generate the predefined displacement input for the experimental assessment. The diagonal braces are assumed to be axially

Table VI. Input data for validation of MR damper models.

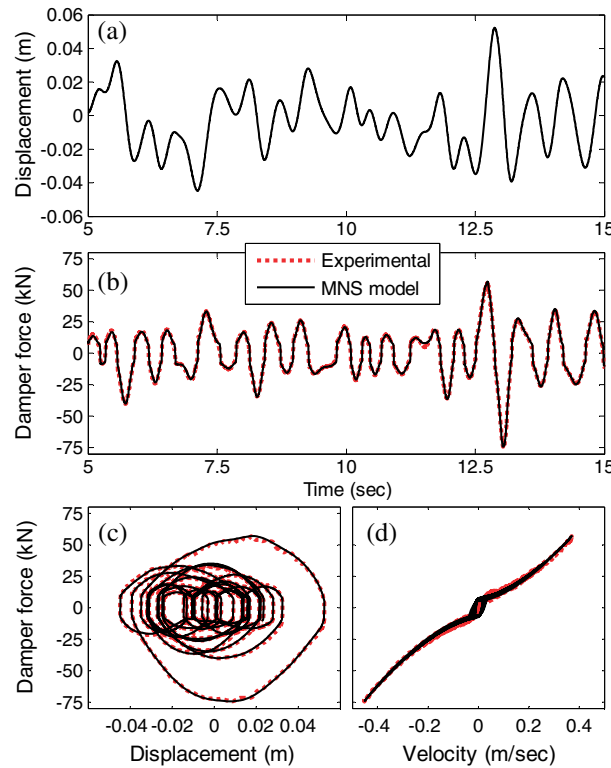| Damper displacement input	Current (A)	Maximum displacement (m)	Maximum velocity (m/s)	Bandwidth (Hz)
Gaussian white noise	0.0	0.052	0.452	2
	2.5	0.031	0.495	4
Earthquake response	2.5	0.056	0.499	—

Figure 12. Comparison of predicted damper force by MNS model with experimental data (I = 0.0 A, Gaussian white noise input – 2 Hz bandwidth): (a) time history of displacement; (b) time history of damper force; (c) force–displacement relationship; and (d) force–velocity relationship.

rigid and the shear building (without MR dampers) is assumed to have 5% viscous damping ratios for modes 1 and 2. The 1994 Northridge earthquake record from the Canoga Park station (360 component) is used as the ground motion. By utilizing the procedure proposed by Somerville *et al.* [26], the ground motion is scaled up by a factor of 3.33 to simulate the intensity of the DBE, where the variables for the DBE response spectrum are chosen as S_{DS}=1.0 g and S_{DI}=0.6 g based on the deterministic limit for the maximum considered earthquake ground motion [27]. The DBE has a 10% probability of exceedance in 50 years; and is approximately two-thirds the intensity of the maximum considered earthquake that has a 2% probability of exceedance in 50 years [28]. It is assumed that there are eight dampers in the 1st story and one damper in the 2nd story of the structure, with each having a constant current of I = 2.5A, to achieve a maximum design story drift of less than 1.5% under the DBE in accordance with the simplified design procedure of Chae *et al.* [13]. The maximum story drifts of the building from time history analysis are 1.22% and 0.85% for the 1st and the 2nd stories, respectively. Figure 15 shows the displacement history of the 1st story MR damper from the time history analysis. This displacement history is then imposed on the damper in the laboratory test setup by the servo-hydraulic actuator with a current input of I = 2.5 A to obtain the experimental damper force response history under an earthquake-generated displacement history. To eliminate any possible displacement error from a delayed response of the hydraulic actuator, the measured displacement of the damper in the test setup is used as the input for the MNS model. The MNS model was then used to predict the damper force response history under the same displacement history. Figure 16 compares the damper force response history from the experiment with that predicted by the MNS model. Shear thinning behavior is observed in the experimental data (see Figure 16(c)) and is accurately predicted by the MNS model. As shown in Figure 16, the predicted damper force by the MNS model matches well with the experimental damper force.

The normalized RMS error for the damper force and the predicted maximum (minimum) damper forces from the MNS model and those from the modified Bouc–Wen and the hyperbolic tangent
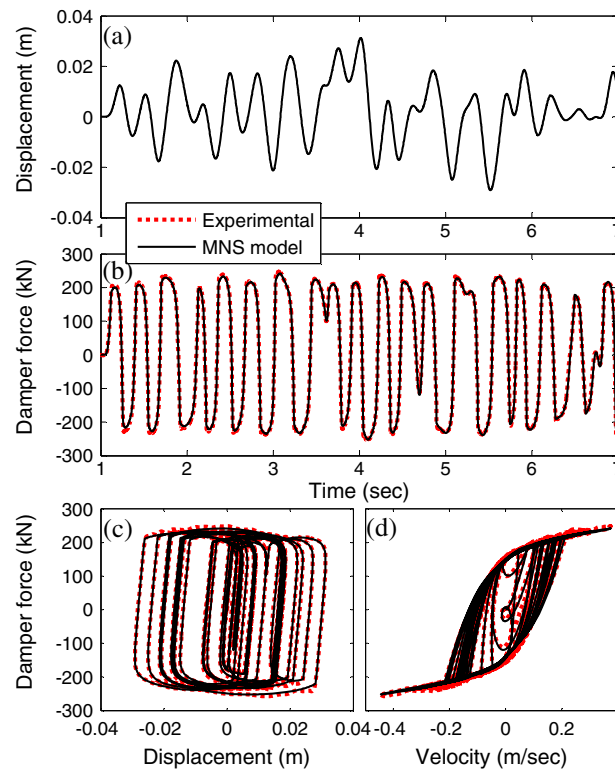
Figure 13. Comparison of predicted damper force by MNS model with experimental data ($I = 2.5$ A, Gaussian white noise input– 4 Hz bandwidth): (a) time history of displacement; (b) time history of damper force; (c) force–displacement relationship; and (d) force–velocity relationship.
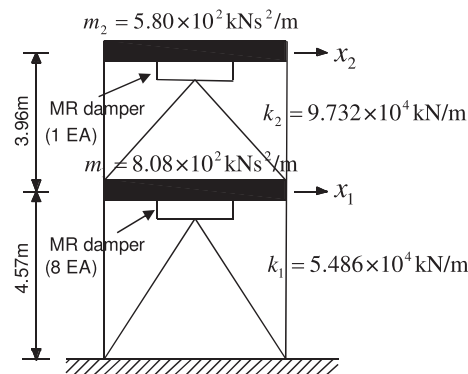

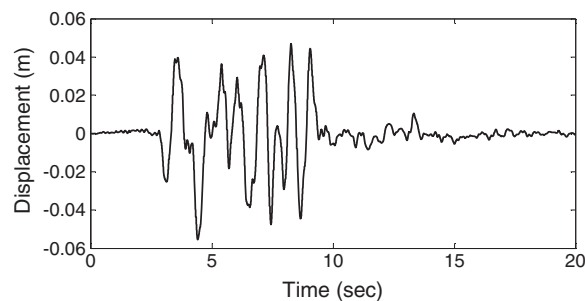Figure 14. Two-story shear building structure with MR dampers.

Figure 15. Displacement history of MR damper in the 1st story from time history analysis.
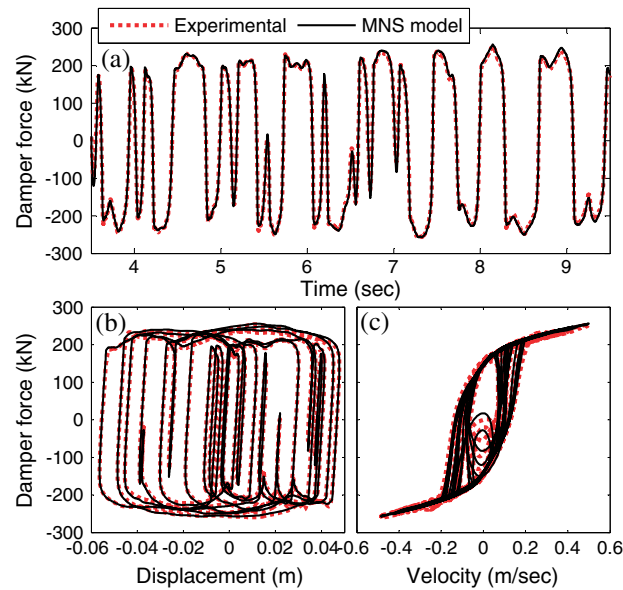

Figure 16. Comparison of predicted damper force by MNS model with experimental data based on earthquake response input (I = 2.5 A): (a) damper force time history; (b) force–displacement relationship; (c) force–velocity relationship.

models are compared in Tables VII and VIII. The MNS model shows a smaller normalized RMS error in Table VII. Moreover, the maximum and minimum damper forces of the MNS model in Table VIII exhibit less discrepancy from the experimental results than the results from the modified Bouc–Wen and hyperbolic tangent models. This latter observation is due to the fact that the post-yield behavior of the modified Bouc–Wen and hyperbolic tangent models is dominated by the linear dashpot c_0 (see Figure 2) that does not model the non-Newtonian behavior of the MR fluid, whereas the

Table VII. Comparison of normalized RMS force error of MR damper models.

Damper displacement input	Current input (A)	Normalized RMS error		
		Modified Bouc–Wen model	Hyperbolic tangent model	MNS model
Gaussian white noise	0.0	0.1291	0.0992	0.0688
	2.5	0.0420	0.0409	0.0370
Earthquake response	2.5	0.0473	0.0528	0.0465

Table VIII. Comparison of minimum and maximum damper force of MR damper models.

Damper displacement input	Current input (A)		Experimental damper force (kN)	Predicted damper force (kN)		
				Modified Bouc-Wen model	Hyperbolic tangent model	MNS model
Gaussian white noise	0.0	Min	−74.1	−61.2 (−17.5%)[a]	−59.2 (−20.1%)	−74.2 (0.1%)
		Max	63.4	54.3 (−14.4%)	53.2 (−16.0%)	64.4 (1.5%)
	2.5	Min	−259.1	−271.4 (4.7%)	−267.9 (3.4%)	−258.3 (−0.3%)
		Max	261.0	268.7 (3.0%)	266.2 (2.0%)	254.6 (−2.4%)
Earthquake response	2.5	Min	−260.0	−269.4 (3.7%)	−265.1 (2.1%)	−257.1 (−1.0%)
		Max	254.0	272.0 (7.1%)	269.3 (6.1%)	256.3 (0.9%)

[a]Numbers in parenthesis denote the percent difference compared with the experimental force.

formulation for the MNS model captures this behavior. These results demonstrate the improved performance of the MNS model over these existing damper models.

6. SUMMARY AND CONCLUSIONS

A newly developed MR damper model called the Maxwell Nonlinear Slider model has been introduced for the prediction of the dynamic behavior of a large-scale MR damper under seismic input. In the MNS model the pre-yield and post-yield behaviors of the MR damper are independently described. This separation makes it easy to estimate model parameters from characterization test data. The MNS model utilizes Hershel–Bulkley visco-plasticity theory to describe the post-yield behavior, which has the ability to account for shear thinning or shear thickening behavior of the MR fluid. This feature of the MNS model is not possessed by the existing modified Bouc–Wen and hyperbolic tangent models. The MNS model exhibits good agreement with experimental data from the characterization tests, and tests with band limited Gaussian white noise input and earthquake induced displacement input. The agreement is good for both pre-yield and post-yield behavior. The MNS model is shown to be overall more accurate than the modified Bouc–Wen and hyperbolic tangent models. Further validation of the MNS model applied to a tall building and a 3-story structure through real-time hybrid simulations is provided in references [21, 29, 30], where various earthquake ground motions scaled to different seismic hazard levels and nonlinear structural response are considered.

REFERENCES

1. Han YM, Nam MH, Han SS, Lee HG, Choi SB. Vibration control evaluation of a commercial vehicle featuring MR seat damper. *Journal of Intelligent Material Systems and Structures* 2002; **13**:575–579.
2. Stelzer GJ, Schulz MJ, Kim J, Allegagn J. A magnetorheological semi-active isolator to reduce noise and vibration transmissibility in automobiles. *Journal of Intelligent Material Systems and Structures* 2003; **14**:743–765.
3. Carlson JD, Catanzarite DM, St Clair KA. Commercial magneto-rheological fluid devices. *Proc. 5th Int. Conf. on ER Fluids, MR Fluids and Associated Tech.*, U. Sheffield, UK, 1995.
4. Dyke SJ, Spencer BF Jr, Sain MK, Carlson JD. Modeling and control of magnetorheological dampers for seismic response reduction. *Smart Materials and Structures* 1996; **5**:565–575.
5. Xu YL, Qu WL, Ko JM. Seismic response control of frame structures using magnetorheological/electrorheological dampers. *Earthquake Engineering and Structural Dynamics* 2000; **29**:557–675.
6. Schurter KC, Roschke PN. Neuro-fuzzy control of structures using acceleration feedback. *Smart Materials and Structures* 2001; **10**:770–779.
7. Ribakov Y, Gluck J. Selective controlled base isolation system with magnetorheological dampers. *Earthquake Engineering and Structural Dynamics* 2002; **31**:1301–1324.
8. Moon SJ, Bergman LA, Voulgaris PG. Sliding mode control of cable-stayed bridge subjected to seismic excitation. *ASCE Journal of Engineering Mechanics* 2002; **129**:71–78.
9. Bani-Hani KA, Sheban MA. Semi-active neuro-control for base- isolation system using magnetorheological (MR) dampers. *Earthquake Engineering and Structural Dynamics* 2006; **35**:1119–1144.
10. Johnson EA, Baker GA, Spencer BF, Fujino Y. Semiactive damping of stay cables. *ASCE Journal of Engineering Mechanics* 2007; **133**(1):1–11.
11. Carlson JD, Spencer BF Jr. Magneto-rheological fluid dampers for semi-active seismic control. *Proc. 3rd Int. Conf. on Motion and Vibration Control*, Chiba, Japan, 1996, 3; 35–40.

12. Yang G. Large-scale magnetorheological fluid damper for vibration mitigation: modeling, testing and control. *Ph.D dissertation*, Department of Civil Engineering and Geological Sciences, University of Notre Dame, Notre Dame, Indiana, 2001.
13. Chae Y, Ricles JM, Sause R. Performance-based design and assessment of structures with magneto-rheological dampers. *ATLSS Report No. 11–01*, Lehigh University, Bethlehem, PA, 2011.
14. Sodeyama H, Suzuki K, Sunakoda K. Development of large capacity semi-active seismic damper using magneto-rheological fluid. *JSME Journal of Pressure Vessel Technology* 2004; **126**:105–109.
15. Bass BJ, Christenson RE. System identification of a 200 kN magneto-rheological fluid damper for structural control in large-scale smart structures. *Proc. American Control Conf.*, New York, 2007.
16. Spencer BF Jr, Dyke SJ, Sain MK, Carlson JD. Phenomenological model for magnetorheological dampers. *ASCE Journal of Engineering Mechanics* 1997; **123**:230–238.
17. Butz T, Von Stryk O. Modelling and simulation of electro- and magnetorheological fluid dampers. *Journal of Applied Mathematics and Mechanics* 2002; **82**:3–20.
18. Gavin HP. Multi-duct ER dampers. *Journal of Intelligent Material Systems and Structures* 2001; **12**:353–366.
19. Wang X, Gordaninejad F. Study of field-controllable, electro- and magneto- rheological fluid dampers in flow mode using Herschel-Bulkley theory. *Proc., SPIE's 7th Annual Int. Symposium on Smart Structures and Materials*, 2000; 232–243.
20. Lee DY, Wereley NM. Analysis of electro- and magneto- rheological flow mode dampers using Herschel-Bulkley model. *Proc. SPIE's 7th Annual Int. Symposium on Smart Structures and Materials*, 2000; 244–255.
21. Chae Y. Seismic hazard mitigation of building structures using magneto-rheological dampers. *Ph.D. Dissertation*, Department of Civil and Environmental Engineering, Lehigh University, Bethlehem, PA, 2011.
22. Kennedy J, Eberhart RC. Particle swarm optimization. *IEEE Int. Conf. on Neural. Networks*, Perth, 1995; 4, 1942–1949.
23. Ye M, Wang X. Parameter estimation of the Bouc-Wen hysteresis model using particle swarm optimization. *Smart Materials and Structures* 2007; **16**:2341–2349.
24. Wen YK. Method for random vibration of hysteretic systems. *Journal of the Engineering Mechanics Division* 1976; **102**(2):249–263.
25. Yang G, Spencer BF Jr, Carlson JD, Sain MK. Large-scale MR fluid dampers: modeling and dynamic performance considerations. *Engineering Structures* 2002; **24**:309–323.
26. Somerville P, Smith N, Punyamurthula S, Sun J Development of ground motion time histories for phase 2 of the FEMA/SAC steel project. *Report No. SAC/BD-97/04, SAC Joint Venture*, Sacramento, CA, 1997.
27. International Code Council. International building code. Falls Church, VA, 2003.
28. FEMA. NEHRP Recommended Provisions for Seismic Regulations for New Buildings and Other Structures. Part 1 - Provisions and Part 2 – Commentary. FEMA 450, Federal Emergency Management Agency, Washington, D.C., 2003.
29. Chae Y, Tong S, Marullo T, Ricles JM. Real-time hybrid simulation studies of complex large-scale systems using multi-grid processing. *20th Analysis and Computation Specialty Conference*, Chicago, IL, 2012.
30. Chae Y, Ricles JM, Sause R. Modeling of a large-scale magneto-rheological damper for seismic hazard mitigation, part II: semi-active mode. *Earthquake Engineering and Structural Dynamics* 2012. DOI: 10.1002/eqe.2236